A multicontrast MR atlas of the Wistar rat brain

G. Allan Johnson[a,b,*], **Rick Laoprasert**[a], **Robert J. Anderson**[a], **Gary Cofer**[a], **James Cook**[a], **Forrest Pratson**[a], **Leonard E. White**[c]

[a]Center for In Vivo Microscopy, Department of Radiology, Duke University Medical Center, Durham, NC 27710, USA

[b]Department of Biomedical Engineering, Duke University, Durham, NC 27710, USA

[c]Department of Neurology, Duke University Medical Center, Durham, NC 27710, USA

Abstract

We describe a multi-contrast, multi-dimensional atlas of the Wistar rat acquired at microscopic spatial resolution using magnetic resonance histology (MRH). Diffusion weighted images, and associated scalar images were acquired of a single specimen with a fully sampled Fourier reconstruction, 61 angles and b=3000 s/mm^2 yielding 50 um isotropic spatial resolution. The higher angular sampling allows use of the GQI algorithm improving the angular invariance of the scalar images and yielding an orientation distribution function to assist in delineating subtle boundaries where there are crossing fibers and track density images providing insight into local fiber architecture. A multigradient echo image of the same specimen was acquired at 25 um isotropic spatial resolution. A quantitative susceptibility map enhances fiber architecture relative to the magnitude images. An accompanying multi-specimen atlas (n=6) was acquired with compressed sensing with the same diffusion protocol as used for the single specimen atlas. An average was created using diffeomorphic mapping. Scalar volumes from the diffusion data, a T2* weighted volume, a quantitative susceptibility map, and a track density volume, all registered to the same space provide multiple contrasts to assist in anatomic delineation. The new template provides significantly increased contrast in the scalar DTI images when compared to previous atlases. A compact interactive viewer based on 3D Slicer is provided to facilitate comparison among the contrasts in the multiple volumes. The single volume and average atlas with multiple 3D volumes provide an improved template for anatomic interrogation of the Wistar rat brain. The improved contrast to noise in the scalar DTI images and the addition of other volumes

*Corresponding author at: Duke University, Center for In Vivo Microscopy, Department of Radiology, DUMC Box 3302, Durham, NC, 27710, USA., gjohnson@duke.edu, tatiana.johnson@duke.edu (G.A. Johnson).

(eg. QA,QSM,TDI) will facilitate automated label registration for MR histology and preclinical imaging.

Keywords

MR histology; MR microscopy; Rat brain; Diffusion tensor imaging; Atlas

1. Introduction

Atlases have played a crucial role in brain research by providing a common map and ontology allowing investigators to compare their findings. There are numerous atlases of the rat brain. One of the most widely cited is "The Rat Brain in Stereotaxic Coordinates" by Paxinos and Watson, which is based on postmortem, two-dimensional histology sections (Paxinos and Watson, 2013). The development of MRI created the opportunity to image the brain intact in the skull without distortion or the introduction of physical artifacts associated with dissection, fixation and sectioning. The first three-dimensional (3D) MR atlas of the rat brain was published in 1987 with spatial resolution of $115 \times 115 \times 1200$ um (voxel volume of 0.016 mm^3) (Johnson et al., 1987). Continued technical developments have led to MR atlases with isotropic spatial resolution of 25 um; i.e., voxels that are more than 1,000 times smaller (Johnson et al., 2012; Calabrese et al., 2013). Anatomic definition in the Paxinos/Watson atlas is based on cresyl violet (Nissl) and acetylcholinesterase (histochemical) stains. MR atlases initially relied on differences in spin lattice relaxation (T1) and spin-spin relaxation times (T2) for anatomic definition. More recently, technical advances have opened the door to new sources of tissue contrast based on diffusion and magnetic susceptibility (Basser et al., 1994, Liu). These new sources of contrast will facilitate mapping labels from the atlas to in vivo preclinical images (e.g., MRI, PET and CT) to assist in identifying anatomical structure (Liu et al., 2013; Mikheev et al., 2016; Johnson et al., 2018). Our major use for the atlas is automated label mapping for MR Histology (Johnson et al., 1993). Examples of this use can be found in studies of traumatic brain injury (Calabrese et al., 2014), neurotoxicology (Johnson et al., 2014; Sills et al., 2004) and genetics (Antonsen et al., 2013; Wang et al., 2020).

Table 1 provides a summary of MR atlases of the rat brain published to date. These include both *in vivo* and *ex vivo* studies at widely varying spatial resolution and widely varying tissue contrast. Definition of spatial resolution is nuanced by the effective slice thickness, slicing interval, degree of voxel isotropy, and resolution in-plane. We have included the Paxinos/Watson atlas (Paxinos and Watson, 2013) for reference where the in-plane resolution for the printed photomicrographic plates is ~ 1 um with 40 um thick sections taken at 120 um intervals. The images in the new MR template reported here were acquired with isotropic spatial resolution of 25 um and 50 um.

Contrast resolution can be as important as spatial resolution in identifying anatomic boundaries. Several atlases of the rat brain have demonstrated the value of diffusion weighted imaging in defining anatomic boundaries (Johnson et al., 2012; Calabrese et al., 2013; Calabrese and Johnson, 2013; Papp et al., 2014; Kjonigsen et al., 2015; Osen et al.,

2019). The new template reported here, has increased the contrast resolution by increasing the angular sampling by 10-fold (n=61) and the diffusion weighting to 3000 s/mm^2. This new template uses the increased sampling and diffusion weighting to generate improved scalar images derived from the DTI algorithm [i.e., axial diffusivity (AD), radial diffusivity (RD), mean diffusivity (MD), fractional anisotropy (FA), color fractional anisotropy (clrFA). The increased angular sampling allows one to use the generalized q sampling imaging (GQI) algorithm (Yeh et al., 2010) to generate additional image volumes to assist in anatomic definition – the quantitative anisotropy (QA) and its associated color version (clrQA). The orientation distribution function (ODF) derived from the GQI algorithm provides another metric that can help define boundaries in areas with complex fiber architecture. The track density image (TDI) derived from the GQI algorithm provides additional insight into local fiber architecture. Finally, a new volume derived from the quantitative susceptibility map (QSM) provides an additional aid for anatomic delineation. Previous atlases have focused on a single specimen. This new template also provides a population average (n=6). The improved contrast to noise in the scalar DTI images and the addition of other volumes (eg. QA,QSM,TDI) will facilitate automated label registration for MR histology and preclinical imaging (Sharief et al., 2008). Finally, we have bundled all the data into a digital application allowing users to interactively explore all these features in a single workspace.

2. Materials and methods

2.1. Specimen preparation

All animal procedures were approved by the Duke IACUC. Male Wistar rats weighing 345–374 gm were purchased from Jackson Laboratories. The weight of the animal from which the single brain atlas was generated was 345.6 gm. The average atlas was generated from six specimens with mean weight (± SD) of 361.0 ± 7.5 gm. Brains were perfused using the active staining protocol described previously (Johnson et al., 2012; Johnson and Hedlund, 2000; Johnson et al., 2002). Briefly, the brain was perfused *in situ* with a mixture of buffered formalin and 10% Prohance (Gadoteridol; Bracco Diagnostics Inc., Monroe Twp., NJ, USA). The head was removed and placed in buffered formalin for 24 hrs. The intact skull was moved to a 0.5% Prohance/normal saline solution to rehydrate the tissue. Tissue was allowed to equilibrate for at least three weeks prior to imaging. The brain was imaged in the skull.

2.2. Image acquisition

Imaging was performed on a 7 T / 210 mm horizontal bore magnet (Magnex Scientific, Yarnton, Oxford, UK) equipped with gradient coils providing 650 mT/m (Resonance Research, Inc., Billerica, MA, USA), and controlled with an Agilent Direct Drive console. A 30 mm diameter x 50 mm long solenoid rf coil constructed from a single sheet of silver foil was constructed to provide uniform excitation and high sensitivity. Volumes for two atlases were acquired. The single-specimen atlas was acquired with full Fourier space sampling. Multi-gradient refocused echo (MGRE) images were generated using a 3D Cartesian encoded sequence with readout gradient along the long axis of the specimen (TR=75 ms, TE=8.6 ms, NEX=2, a=60°, 4 echoes). The acquisition matrix for the single specimen was $1600 \times 800 \times 800$ with a field of view of $40 \times 20 \times 20$ mm yielding a

Nyquist spatial resolution of 25 μm. The aggregate volume of the four-dimensional (4D) magnitude data set was 4 GB. Diffusion-weighted images were acquired using a Stejskal/ Tanner spin-echo sequence (TR=100 ms, TE=22.5 ms) with a pair of unipolar, half-sine diffusion gradients (600 mT/m) on either side of the refocusing rf pulse yielding a b value of 3000 s/mm^2 (Stejskal and Tanner, 1965; Jiang and Johnson, 2010). Sixty-one volumes were acquired in a single shell with angular samples distributed uniformly on the unit sphere. Six baseline (b0) images were acquired spaced uniformly throughout the scan period. The total scan time for the diffusion set was 289 hours. The aggregate volume of the 4D magnitude data set was 16 GB.

Six additional specimens were scanned for a population atlas using a streamlined protocol. The acquisitions were accelerated by reducing the field of view ($18 \times 18 \times 36$ mm), still maintaining 50 um isotropic resolution, reducing the angular sampling to 46 angles with 5 baseline images and using compressed sensing (compression of 8X), as described more fully in ref Wang et al. (2018). Weighting for the diffusion weighted scans was identical to the single-specimen acquisition (b= 3000 s/mm^2).

2.3. Post processing

The four echoes from the MGRE of the single specimen atlas were summed to improve contrast and signal to noise. A QSM was generated on each of the individual 4 echoes using the methods described in Liu et al. (2011). The resulting individual susceptibility images were summed to yield the QSM in the atlas.

Diffusion data were processed with an image-processing pipeline comprised of open source software packages, including Perl (http://www.perl.org), ANTs (http://www.picsl.upenn.edu/ ANTS/), and DSI Studio (http://dsi-studio.labsolver.org/). The first step of the pipeline generated an average baseline image by registering all the b0 images together. The diffusion weighted images were then registered to this average. The resulting 4D volume was loaded into DSI Studio for diffusion and tract generation. The data were processed using both the DTI and GQI algorithm (Yeh et al., 2010) yielding the following scalar images: AD, FA, MD, RD, QA, clrQA, and DWI. The 4D arrays from the six specimens in the average atlas were registered together using the Q space diffeomorphic reconstruction (QSDR) algorithm of DSI Studio from which the same scalar images were then generated within DSI Studio (Yeh and Tseng, 2011). Imaris (https://imaris.oxinst.com/) was used for multimodal combined visualization.

2.4. Anatomic delineation

Our goal was to produce an atlas suitable for machine-driven label mapping onto rat brains under study with quantitative MR histology. The robustness of most automated registration schemes is dependent on the signal and contrast to noise in the underlying template. We have previously demonstrated that the use of multiple (registered) volumes with different sources of image contrast can significantly improve automated label mapping (Badea et al., 2012; Anderson et al., 2019). Thus, our anatomic delineations have been generated with the help of the multiple scalar volumes and consistency across those volumes.

Delineations were aided by using complimentary contrast from multiple scalar images (AD, DWI, GRE, MD, QA, clrQA, RD and b_0). All volumes in registration were loaded into Avizo (https://www.fei.com/software/avizo3d/\045C2\045A0#gsc.tab=0) configured to display three orthogonal planes. Aviso provides the user the capacity to toggle among volumes. Our strategy was to construct delineations based on the contrast available across multiple scalar images, with reference to previous work and reliance on the data volume providing the clearest demonstration of relevant anatomical boundaries. For example, QA and GRE typically yielded the strongest contrasts for defining the boundaries between gray matter and white matter structures, while DWI and RD often yielded excellent contrasts for differentiating compact cellular structures, such as the pyramidal and granule cell layers of the hippocampus (see Fig. 4). In cases where the boundary was poorly defined with one image contrast, the user toggled to any of the others for clarity. A detailed description of the process, illustrating delineation of the ventral posterior complex of the thalamus, is included in the Supplement (Figs. S1–S7). Quality assurance was performed during a weekly review of delineations with an expert neuroanatomist (LEW). The Allen Brain Atlas ontology was used to organize our delineations by neuroanatomical region and to provide consistency with the expanding use of the ABA digital mouse atlas. The complete list of delineated structures and their organization by region is included in Table S1 of the Supplement.

2.5. Symmetric atlas labels

The labels were symmetrized using an intermediate average constructed from the original DWI image and an image in which the right hemisphere was reflected into the left hemisphere. The SAMBA registration pipeline, built on ANTs was used to create a symmetric template using both affine and diffeomorphic transforms (Anderson et al., 2019). The labels were similarly reflected and mapped to this template. The original image was diffeomorphically registered to this symmetrized template to allow transformation of the symmetric labels.

2.6. Fiber tracking

Calamante et al. have demonstrated that tract density images (TDI) can provide useful anatomic content to compliment the other scalar images generated in DSI studio (Calamante et al., 2010, 2012). The .fib file generated in DSI Studio lays the foundation for future extension in quantitative connectomics. Tractography was generated using the GQI algorithm (Yeh et al., 2010) with the following tracking parameters: threshold=0.075, angular threshold=60, step size=0.01, smoothing=0.01, minimum length=0.5 mm, maximum length=800 mm, seed orientation was random, seed position was subvoxel, randomize seeding was on, direction interpolation was trilinear, and the tracking algorithm was RK4. The maximum total number of streamlines was 8×10^6. This produced a QA image, which is similar to the FA image. TDIs were generated using the method describe by Calamante et al. (2010, 2012) with whole-brain seeding.

3.   Results

3.1.   Increased signal- and contrast-to-noise help define neuroanatomical detail

Fig. 1 shows the major advance in this template through the improved signal- and contrast-to-noise. Fig. 1A from our previous work on the Wistar rat (Johnson et al., 2012) shows a coronal plane through the FA volume at 50 um isotropic resolution. Fig. 1B shows a comparable slice from WHS 1 of a Sprague Dawley rat at 78 um also acquired in our laboratory (Papp et al., 2014). The data in 1A and 1B were acquired with methods that were state of the art at that time (6 angles, b~ 1462 s/mm^2). Fig. 1C from this new template demonstrates the dramatic improvement in contrast to noise derived from the increase in b (3000 s/mm^2) and ten-fold increase in angular sampling (n=61).

Fig. 2 shows a comparison between the MGRE image derived by summing all four echoes (A), a Nissl section from the Paxinos Watson (PW) atlas (B), the QSM image constructed from all four echoes in the MGRE (C), and an acetylcholinesterase section from the PW atlas (D) all at the same axial level (with the acetylcholinesterase section in the same section series as the Nissl section Paxinos and Watson, 2013). The plane of the atlas images (A and C) was angled to match the plane of the Nissl section (plate 198 @ bregma −5.32 mm) from the PW atlas (B) using multiple intrinsic landmarks (Johnson et al., 2012; Calabrese et al., 2013). The acetylcholinesterase section (D) (plate 199 @ bregma −5.10) is a slice from the same series of sections, with a separation of 220 um between (B) and (D). The PW sections are 40 um-thick and the two MR images were generated from the same 25 um axial plane.

One of the most obvious benefits of the MR atlas is the fact that the brain is still in the cranial vault at the time of imaging so there is no geometric distortion attributable to cranial dissection or section mounting and no artifact of tissue sectioning and/or histological/ histochemical processing (as is apparent in even the very best histological atlases; see Fig. 2B and D). To facilitate use of the template in machine-driven registration, the skull has been digitally stripped in the MR atlas; however, the skull is still physically in place so the soft tissue sections remain registered to bregma. Note that the sections in B and D are expanded laterally relative to the MR images in A and C. This lateral expansion could be due to individual differences in brain morphology among individuals. However, it is more likely an artifact of postmortem cranial dissection and tissue processing. Similarly, there appear to be postmortem changes in the shape and aspect ratio of the cerebellum, when histological sections are compared to MR atlas images.

Fig. 3 shows a magnified section of the same level through the hippocampus for A (sum of four echoes in the MGRE) and B (Nissl) from Fig. 2. The spatial resolution of the Nissl (B) is a function of conventional light microscopy and photomicrographic reproduction and therefore clearly greater than that of the MGRE. Furthermore, the Nissl stain is, by design, differentiating the presence of Nissl substance (rough endoplasmic reticulum and granules associated with ribonucleic acid) in cell bodies and nucleoli from the unstained matrix of neuropil (tissue volume other than cell bodies). The MGRE at 25 um resolution is sufficient to resolve other structures in the tissue, including several landmarks in the Nissl section and some that are differentiated more clearly in the MGRE image: 1) the external capsule, a subcortical white matter structure; 2) the alveus, a white matter structure originating

in the lateral and anterior margins of the hippocampus; 3) the hippocampal fissure, a developmental remnant of the occluded space between the dentate gyrus and the CA1 division of the hippocampus; 4) the optic radiation, a distinct tract of white matter emanating from the lateral geniculate complex of the thalamus; and 5) fascicles of myelinated axons (white matter fibers) in the ventral-lateral thalamus coursing towards the internal capsule. These boundary definitions are more evident in the MGRE than in a standard Nissl-stained section because of the higher contrast between gray matter and white matter in the MGRE image. The clearer boundary in the MR template is particularly relevant for automated registration.

Fig. 4 expands on the different tissue contrasts accessible in this atlas. Even though the spatial resolution in the diffusion scalars (50 um) is lower than that of the MGRE (25 um), the intrinsic contrast is considerably higher. The coronal section is roughly equivalent to plate 72 at bregma −4.68 mm in the PW atlas (Paxinos and Watson, 2013) and plate 49 at bregma −4.86 mm in the more recent MRI/DTI atlas (Paxinos et al., 2015). The higher resolution in the MGRE (Fig. 4A) resolves gray/white matter boundaries and bundles of axon fascicles penetrating diencephalic (thalamic) gray matter; but the increased sensitivity to cellular density in Fig. 4B, the diffusion weighted image, highlights the granular layer of dentate gyrus and the pyramidal cell layers of the hippocampus, which are barely visible in the MGRE. The cell-sparse layers of the dentate gyrus and hippocampus—in particular, the molecular layer of the dentate gyrus and the stratum radiatum of the CA1 field—are well-differentiated in Fig. 4C, the AD image. In Fig. 4D, the RD image, many features evident in other contrasts (e.g., DWI and QA) are clearly recognizable, such as the cell-dense layers of the dentate gyrus and the hippocampal CA-fields and the compact white matter of the corpus callosum, while differentiation of other features appears clearer, such as the white matter tracts bounding the substantia nigra. One interesting feature to note across contrasts is the stark inversion of contrast in the fasciculus retroflexus between the AD and RD images (cf. Fig. 4C and D), while differentiation of the cell-sparse hippocampal layers is reduced. The QA image, Fig. 4E is one of the most easily interpreted MR contrasts since white matter has a high anisotropy and compact white matter structures, such as the corpus callosum and external capsule, are readily discerned. Note the differentiation of the cerebral peduncle from the substantia nigra, an aspect of mesencephalic anatomy not seen as clearly in the DWI or AD images. Finally, the clrQA, Fig. 4F, reveals additional anatomical components of structures based on the orientation of anisotropic diffusion signal. The most recognizable features highlighted in this image are the transversely oriented (red) fibers in the corpus callosum that cross the midsagittal plane. Just dorsal to these fibers are the bilateral cingulum bundles that are colored green, reflecting their longitudinal orientation orthogonal to the underlying callosal fibers. Also, note the differentiation of radial cytoarchitecture in the upper layers of the neocortex (blue in dorsal neocortical areas and red in more lateral areas).

3.2. There is good agreement between single and average atlas

Fig. 5 shows representative DWI (Fig. 5A) and QA (Fig. 5B) images obtained at the same level. In each panel, the section shown is a composite facilitating comparison of an image from the single-brain atlas (left side of each section) and an image from the corresponding

coronal level from the population atlas (n=6) (right side of each section). In the generation of the population atlas, the alignment of datasets from the six different brains was surprisingly good, presumably because of their uniform strain and sex, and the fact that they were imaged *in situ*. Inspection of the intrinsic features of left and right sides of the DWI and QA images demonstrates little loss of structural detail from alignment. One significant difference in the average DWI image compared to the single-brain image is the degradation of contrast in the granular cell layer of the dentate gyrus. Otherwise, among the only noticeable differences between the single-brain DWI image and the average DWI image is some blurring in the average image in regions where one should expect interindividual variation (even within the same strain), such as blood vessels in the hippocampal fissure and choroid plexus in the lateral ventricle. Similarly, in the average QA image, there is little evidence of degradation in contrast associated with any brain structure. Thus, the interactive atlas application (described below) accurately presents the anatomical features present in an average Wistar rat brain with state-of-the-science spatial and contrast resolution.

3.3. Coordinate system

The origin of the coordinate system has been defined at the midline and juncture between anterior and posterior segments of the anterior commissure as demonstrated in Fig. 6. The angulation of the volumes was defined in collaboration with Professors George Paxinos and Charles Watson to match the coronal plane of their atlas (Paxinos and Watson, 2013). The process described in detail in Johnson et al. (2012) relies on three landmarks (medial cerebellar nucleus; ventral-most aspect of the genu of the corpus callosum; ventral-most aspect of the posterior commissure) which are visible in the PW horizontal sections. The angle of the axis defining the axial planes in the MR data was iteratively adjusted until the landmarks in the axial MR images matched those in the three adjacent axial slices of the Paxinos-Watson data. Agreement between the two can be seen in Fig. 7.

3.4. Anatomic delineations

Our goal was to produce a set of anatomic delineations that would be useful for whole-brain MR histology including connectomic analysis of DTI-derived tracts in the rat brain. Toward that goal, we identified a total of 139 relevant structures in each hemisphere (see below), with an additional 9 structures that account for ventricular compartments and voxels not otherwise assigned to discrete brain structures. Cortical areas, subcortical gray and white matter structures, and compact white matter tracts were delineated when one or more MR volumes (typically, DWI and FA) presented evidence of boundary conditions that enabled differentiation of contiguous brain areas and structures. Preparing a set of delineations that would facilitate subsequent tractography and connectomics analysis led to practical compromises between useful delineations for connectomics and high-resolution definition of additional anatomic detail. Thus, we did not attempt to create an exhaustive compilation of all recognizable structural detail evident in our volumes. Refining and increasing delineations will remain an ongoing development for ourselves and the community of users of our atlas application.

3.5. Interactive atlas application

Fig. 7 provides a screen capture of the atlas application that allows exploration of rat brain anatomy interactively using all the different scalar images in the single rat brain and the average atlas. The application is built on 3D Slicer (https://www.slicer.org/). The application and all the data are bundled in PC or Mac specific packages and available at our web site (https://civmvoxport.vm.duke.edu/voxbase/studyhome.php?studyid=754) and NITRC.org (RRID:SCR_001808) The bundles include image data as NRRD files which can be opened in other display packages. Instructions are included in the Supplement. The "Data Package" drop down from the Slicer menu allows one to choose the single or average atlas. The application programming interface is available in Slicer to define other display protocols or layouts. Custom layouts are provided with the atlas application package that display in Slicer a sagittal reference image (MD in this example) in the upper left window to position the navigation planes. Using the scroll function on the mouse allows one to move this plane laterally through different sagittal slices to find landmarks of interest. The scroll bars beneath the window provide indices for position and angle of the coronal sections displayed in the lower panes. A drop-down menu below the lower panes allows one to choose from the multiple volumes available. There are 12 different volumes for the single-brain atlas (AD, b0, ClrQA, ClrTDI, DWI, FA, MD, QA, QSM, RD, T2*, TDI) and 9 for the average-brain atlas (AD, ClrQA, ClrTDI, DWI, FA, MD, QA, RD, TDI). As one navigates through a given volume, an additional volume with different contrast is synchronized; that is, each of the lower panes displays a unique MR image contrast centered on the same image plane.

In the Slicer layout shown in Fig. 7, the window in the upper right pane is reserved for a user's image. In the example shown, the upper right pane is loaded with a Nissl section from the PW atlas (Paxinos and Watson, 2013) taken at bregma −6.12 mm. The user can load images of multiple types and file formats (e.g., a DICOM PET image, an *in vivo* MRI, or some other conventional histological image, etc.). One use-case that we envision is loading an experimental image of interest (e.g., a confocal or light-sheet image of the same or different specimen) followed by interactive navigation with slice position and slice angle to find landmarks that would facilitate optimal alignment of the images available in the atlas with the experimental image. Selecting "Turn on all labels" or "Turn off all labels" below the window in the upper left pane toggles on/off the delineations according to user preference. With delineations on or off, mousing over the displayed image in any volume brings up in the lower left corner of the Slicer window the identifying label for the delineation under the mouse's pointer. Clicking anywhere in a displayed image brings up the delineation and the identifying label for the structure that contains the location of the mouse's pointer when clicked. Repeating the point-and-click routine in adjacent regions allows users to build a display of delineations in a brain region of interest, without necessarily turning all labels on. Clicking a second time in the same region deselects the delineation, as does clicking "Turn off all labels". The application and data are available under the creative commons license (https://creativecommons.org/licenses/by-nc/4.0/).

Supplemental Table S2 summarizes the content in the application.

3.6. Multi-dimensional visualization

The improved signal to noise highlights anatomic features in some of the images not previously seen. Fig. 8A shows a coronal section through the QA volume corresponding to bregma −6.12 mm that was assigned a yellow look-up table for this figure. Fig. 8B at the same level though the AD volume was assigned a green look-up table to differentiate it from the QA. In the QA image, the external capsule (high QA signal) is well-differentiated from the underlying alveus/stratum oriens of the CA1 field of the hippocampus (low QA signal). Further, the proximal apical plexiform layers of the CA1 field (stratum radiatum) and the dentate gyrus (molecular layer) display high levels of signal in the QA image. Presumably, this high QA signal relates to the radial organization of the principal dendrites of the projection neurons in these hippocampal divisions (Amaral et al., 2007). Interestingly, the more distal plexiform layer of the CA1 field (stratum lacunosum-moleculare) is quite low in QA signal, presumably reflecting the more complex cytoarchitecture of this sublaminar division (Maccaferri, 2011). Further, the CA1 pyramidal cell layer and the granule cell layer of the dentate gyrus are likewise poorly differentiated in the QA image. However, both cell-dense layers are more clearly seen in the AD image. Combining the two with different color maps in Fig. 8C merges the features from both contrasts making it possible to distinguish several layers of the hippocampus in a single image, including the cell dense layers and the apical plexiform layers (note the green and gold banding across the hippocampus). This approach to visualizing neuroanatomical structure may be particularly valuable when using this atlas for automated segmentation or machine learning applications.

Track density images (TDI), as described by Calamante et al. (2010), have also been included as an addition to the scalar volumes used to delineate anatomical structure. Gray scale TDI show tracks with signal intensity reflecting the spin density. Color TDI images add color to infer local track orientation. Calamante et al. have demonstrated the value of TDI in anatomical delineation in the mouse (Calamante et al., 2012). Fig. S8 provides an example in which the color TDI are combined with gray scale scalar images to delineate fine structure in the hippocampus and amygdala. As shown in panels A and L, the individual data volumes examined in complimentary display taken together with such novel hybrid (merged-image) visualizations provide a robust platform for harvesting additional delineations of anatomic structure in the Wistar rat brain.

4. Discussion

4.1. Spatial resolution and contrast resolution are both important

The improved contrast-to-noise in multiple volumes in this new template provides significant advances over previous work. Many of the previous atlases are based on a single MR contrast; i.e., T1, T2 or T2*, all of which have been acquired at significantly lower spatial resolution. Wisner et al. have produced one of the highest resolution atlases of this kind (Wisner et al., 2016) with spatial resolution of $50 \times 50 \times 200$ um (voxel volume=0.0005 mm³). The MGRE images in the work reported here (@ 25 um³; i.e., voxel volume=1.5×10^{-5} mm³) have been acquired at 32-times higher spatial resolution. A more recent publication by Barrière et al. report resolution of $90 \times 90 \times 180$ um³ (Barriere et al., 2019). Barrière et al. report a second crucial metric, the contrast resolution. Their formula uses the

standard deviation of all white matter and all gray matter. We have chosen not to employ this metric because the signal-to-noise in these new data is sufficiently high that one can resolve many anatomic structures *within* the gray and white matter, including sublaminar structure in plexiform layers and fascicles of myelinated axons coursing through gray matter. For example, the somatic and neuritic layers in the hippocampus seen in the QA and AD images in Fig. 8 would be counted as noise using their global approach. Fig. 9 shows a comparison at the same level from A) Barrière et al.'s work (Barriere et al., 2019); B) the first echo from the MGRE image in this atlas (@ 25 um isotropic resolution); and C) the registered QA image (@ 50 um isotropic resolution) in this atlas. Barrière et al.'s atlas has been constructed to segment gray matter, white matter, and cerebrospinal fluid. The contrast resolution between gray and white matter is considerably higher in the QA image (Fig. 9C). The contrast-to-noise ratio is sufficient to resolve cortical layers not seen in either A) or B). But closer observation of the olfactory bulb and adjacent anterior olfactory nucleus in the lower half of Fig. 9 shows that layers of the olfactory bulb are visible in B) since the spatial resolution and contrast resolution are sufficient to resolve cytoarchitecture of the bulb. The higher contrast resolution in C) highlights many of the same structures even though the spatial resolution is lower. One of the strengths of this atlas is the combination possible since the volumes are registered.

4.2. This multicontrast atlas is dynamic

MR Histology is becoming much more routine in a wide range of studies in the rat brain (Calabrese et al., 2013, 2014; Johnson et al., 2014; Sills et al., 2004; Calabrese and Johnson, 2013; Antonsen et al., 2013; Sills et al., 2020). The new template and associated labels provided here will facilitate expanded applications. The improved contrast-to-noise, the inclusion of new sources of contrast, (QSM, AD, TDI), and the addition of an average atlas will improve the utility in machine-based registration, facilitate new anatomic delineations, and improvements of existing delineations. Refinement of the coordinate space and consolidating previous work into the interactive application will help harmonize with previous atlases. The new connectome-centric labels and the increased angular sampling lay the ground work for future analyses, including quantitative connectomics. As we and others implement such improvements, they will be made publicly available through updates to the release on NITRC.org, as well as to the atlas application available at our own share site.

5. Conclusion

This is not the last atlas of the rat brain. New imaging methods (e.g., light sheet imaging, optical coherence tomography, further advances in MR imaging and data processing) will provide new insight into the complex micro- and meso-scale organization of the rat brain. And existing atlases will continue to provide the common anatomical framework and ontology for data analyses and dissemination of new discovery. The seven different versions of Paxinos and Watson's atlas stand as a testament to the value of careful scholarship and thorough delineation of neuroanatomical structure. We hope this new multi-contast atlas will assist our understanding of the complex anatomy of the rat brain and that our atlas provides a useful new platform for researchers worldwide.

Supplementary Material

Refer to Web version on PubMed Central for supplementary material.

Acknowledgements

Data and code availability statement

This atlas is available as an open access. Thus, all the anatomic data, registered 4D volumes, delineations and labels, scalar images, and the supporting meta data for this atlas are available under the creative commons framework (cc by-nc-sa 4.0; https://creativecommons.org/licenses/by-nc-sa/4.0/legalcode at) (https://civmvoxport.vm.duke.edu/voxbase/studyhome.php?studyid=754).

Abbreviations:

AD	axial diffusivity
ADC	apparent diffusion coefficient
ClrFA	color encoded fractional anisotropy
DTI	Diffusion tensor imaging
DWI	diffusion weighted image
FA	Fractional anisotropy
GQI	generalized q sampling imaging
GRE	gradient recalled echo
MD	mean diffusivity
MGRE	multi gradient refocused echo
ODF	orientation distribution function
QA	quantitative anisotropy
QSDR	q space diffeomorphic reconstruction
QSM	quantitative susceptibility map
TDI	track density image

References

Paxinos G, Watson C, 2013. The Rat Brain in Stereotaxic Coordinates 7th Edition, seventh edition Academic Press, New York.

Johnson GA, Thompson MB, Drayer BP, 1987. Three dimensional MR microscopy of the normal rat brain. Magn. Reson. Med 4, 351–365. [PubMed: 3586982]

Johnson GA, et al. , 2012. A multidimensional magnetic resonance histology atlas of the Wistar rat brain. Neuroimage 62 (3), 1848–1856. [PubMed: 22634863]

Calabrese E, et al. , 2013. A quantitative magnetic resonance histology atlas of postnatal rat brain development with regional estimates of growth and variability. Neuroimage 71C, 196–206.

Basser PJ, Mattiello J, LeBihan D, 1994. MR diffusion tensor spectroscopy and imaging. Biophys. J 66 (1), 259–267. [PubMed: 8130344]

Liu C, Susceptibility tensor imaging. Magn. Reson. Med. 63(6): p. 1471–1477.

Liu H, Shen X, Tang H, et al. , 2013. Using MicroPET imaging in quantitative verification of the acupuncture effect in ischemia stroke treatment. Sci. Rep 3, 1070. [PubMed: 23323213]

Maccaferri G, 2011. Modulation of hippocampal stratum lacunosum-moleculare microcircuits. J. Physiol 589, 1885–1891. [PubMed: 21135043]

Mikheev AL, Rusinek J, Ding H, Shin Yu, 2016. Mapping mouse brain with atlas for dynamic microPET studies. J. Nucl. Med 57, 1900.

Johnson GA, et al. , 2018. Whole mouse brain connectomics. J. Comp. Neurol 12, 26.

Johnson GA, et al. , 1993. Histology by magnetic resonance microscopy. Magn. Reson. Q 9 (1), 1–30. [PubMed: 8512830]

Calabrese E, et al. , 2014. Diffusion tensor imaging reveals white matter injury in a rat model of repetitive blast-induced traumatic brain injury. J. Neurotrauma

Johnson GA, et al. , 2014. Quantitative mapping of trimethyltin injury in the rat brain using magnetic resonance histology. Neurotoxicology 42C, 12–23.

Sills RC, et al. , 2004. Contribution of magnetic resonance microscopy in the 12-week neurotoxicity evaluation of carbonyl sulfide in Fischer 344 rats. Toxicol. Pathol 32, 501–510. [PubMed: 15603534]

Antonsen BT, et al. , 2013. Altered diffusion tensor imaging measurements in aged transgenic Huntington disease rats. Brain Struct. Funct 218 (3), 767–778. [PubMed: 22618438]

Wang N, A, R., Ashbrook DG, Gopalakrishnan V, Park Y, Priebe CE, Laoprasert R, Vogelstein JT, Williams RW, Johnson GA, 2020. Variability and heritability of mouse brain structure: microscopic MRI atlases and connectomes for diverse strains. Neuroimage 222.

Calabrese E, Johnson GA, 2013. Diffusion tensor magnetic resonance histology reveals microstructural changes in the developing rat brain. Neuroimage 79, 329–339. [PubMed: 23648962]

Papp EA, et al. , 2014. Waxholm space atlas of the Sprague Dawley rat brain. Neuroimage 97, 374–386. [PubMed: 24726336]

Kjonigsen LJ, et al. , 2015. Waxholm Space atlas of the rat brain hippocampal region: three-dimensional delineations based on magnetic resonance and diffusion tensor imaging. Neuroimage 108, 441–449. [PubMed: 25585022]

Osen KK, I, J., Wennbe AE, Papp EA, Leergaard TB, 2019. Waxholm Space atlas of the rat brain auditory system: three-dimensional delineations based on structural and diffusion tensor magnetic resonance imaging. Neuroimage 199, 38–56. [PubMed: 31100433]

Yeh F, Wedeen VJ, Tseng WYI, 2010. Generalized q-sampling imaging. IEEE Trans. Med. Imaging 29 (9), 1626–1635. [PubMed: 20304721]

Sharief AA, et al. , 2008. Automated segmentation of the actively stained mouse brain using multi-spectral MR microscopy. Neuroimage 39 (1), 136–145. [PubMed: 17933556]

Schweinhardt P, F, P., Olson L, Spenger C, Andersson JLR, 2003. A template for spatial normalisation of MR images of the rat brain. J. Neurosci. Methods 129, 105–113. [PubMed: 14511814]

Schwarz AJ, et al. , 2006. A stereotaxic MRI template set for the rat brain with tissue class distribution maps and co-registered anatomical atlas: application to pharmacological MRI. Neuroimage 32 (2), 538–550. [PubMed: 16784876]

Nie B, et al. , 2013. A rat brain MRI template with digital stereotaxic atlas of fine anatomical delineations in paxinos space and its automated application in voxel-wise analysis. Hum. Brain Mapp 34 (6), 1306–1318. [PubMed: 22287270]

Lancelot S, et al. , 2014. A multi-atlas based method for automated anatomical rat brain MRI segmentation and extraction of PET activity. PLoS One 9 (10), e109113 –10.

Wisner K, et al. , 2016. Ratat1: a digital rat brain stereotaxic atlas derived from high-resolution MRI images scanned in three dimensions. Front. Syst. Neurosci 10 (26).

Barriere DA, et al. , 2019. The SIGMA rat brain templates and atlases for multimodal MRI data analysis and visualization. Nat. Commun 10 (1).

Goerzen D, et al., An MRI-derived neuroanatomical atlas of the Fischer 344 rat brain 2019. 29(4): p. 260–28.

Figini M, et al. , 2015. In vivo DTI tractography of the rat brain: an atlas of the main tracts in Paxinos space with histological comparison. Magn. Reson. Imaging 33 (3), 296–303. [PubMed: 25482578]

Veraart J, et al. , 2011. Population-averaged diffusion tensor imaging atlas of the Sprague Dawley rat brain. Neuroimage 58 (4), 975–983. [PubMed: 21749925]

Osen KK, et al. , 2019. Waxholm Space atlas of the rat brain auditory system: three-di-mensional delineations based on structural and diffusion tensor magnetic resonance imaging. Neuroimage 199, 38–56. [PubMed: 31100433]

Paxinos G, et al., 2015. An MRI/DTI Atlas of the Rat Brain Academic Press, Elsevier, p. 224.

Argyridis I, et al. , 2013. Quantitative magnetic susceptibility of the developing mouse brain reveals microstructural changes in the white matter. Neuroimage 88C, 134–142.

Basser PJ, Pierpaoli C, 1996. Microstructural and physiological features of tissues elucidated by quantitative diffusion tensor MRI. J. Magn. Reson. B 111, 209–219. [PubMed: 8661285]

Mori S, Zhang J, 2006. Principles of diffusion tensor imaging and its applications to basic neuroscience research. Neuron 51 (5), 527–539. [PubMed: 16950152]

Johnson GA and Hedlund LW, Three-Dimensional Morphology by Magnetic Resonance Imaging, Office UP, Editor. 2000, Duke University: U.S.A.

Johnson GA, et al. , 2002. Morphologic phenotyping with magnetic resonance microscopy: the visible mouse. Radiology 222 (3), 789–793. [PubMed: 11867802]

Stejskal EO, Tanner JE, 1965. Spin diffusion measurements: spin echoes in the presence of a time-dependent field gradient. J. Chem. Phys 42 (1), 288.

Jiang Y, Johnson GA, 2010. Microscopic diffusion tensor imaging of the mouse brain. Neuroimage 50 (2), 465–471. [PubMed: 20034583]

Wang N, et al. , 2018. Whole mouse brain structural connectomics using magnetic resonance histology. Brain Struct. Funct 223 (9), 4323–4335. [PubMed: 30225830]

Liu C, et al. , 2011. High-field (9.4T) MRI of brain dysmyelination by quantitative mapping of magnetic susceptibility. Neuroimage 56 (3), 930–938. [PubMed: 21320606]

Yeh F, Tseng WYI, 2011. NTU-90: a high angular resolution brain atlas constructed by q-space diffeomorphic reconstruction. Neuroimage 58, 91–99. [PubMed: 21704171]

Badea A, et al. , 2012. Quantitative mouse brain phenotyping based on single and multi-spectral MR protocols. Neuroimage 63 (3), 1633–1645. [PubMed: 22836174]

Anderson RJ, et al. , 2019. Small animal multivariate brain analysis (SAMBA) – a high throughput pipeline with a validation framework. Neuroinformatics 17 (3), 451–472. [PubMed: 30565026]

Anderson RJ, et al. , Small animal multivariate brain analysis (SAMBA) – a high throughput pipeline with a validation framework. Neuroinformatics: p. 1–22.

Calamante F, et al. , 2010. Track-density imaging (TDI): super-resolution white matter imaging using whole-brain track-density mapping. Neuroimage 53 (4), 1233–1243. [PubMed: 20643215]

Calamante F, Tournier JA, Kurniawan ND, Yang Z, Gyengesi E, Galloway GJ, Reutens DC, Connelly A, 2012. Super-resolution track-density imaging studies of mouse brain: comparison to histology. Neuroimage 59, 286–296. [PubMed: 21777683]

Amaral DG, S., H., Lavenex P, 2007. The dentate gyrus: fundamental neuroanatomical organization (dentate gyrus for dummies). Prog. Brain Res 163, 3–22. [PubMed: 17765709]

Antonsen B, Jian Y, Veraart J, Qu H, Nguyen HP, Sijbers J, vonHorsten S, Johnson GA, Leergaard TB, 2013. Altered diffusion tensor imaging measurements in aged transgenic Huntington disease rats. Brain Struct. Funct 218, 767–778. [PubMed: 22618438]

Sills RC, J, G., Anderson RJ, Johnson CL, Statup M, Brown DL, Churchill SR, Kurtz DM, Cushman JD, Waidyanatha S, Robinson VG, Cesta MF, Andrews DMK, Behl M, Chickley KR, Little PB, 2020. Qualitative and quantitative neuropathology approaches using magnetic resonance microscopy (Diffusion Tensor Imaging) and stereology in a hexachlorophene model of myelinopathy in Sprague-Dawley rats. Toxicol. Pathol 48 (8), 965–980. [PubMed: 33334257]

Barrière D, Magalhães R, Novais A, Marques P, Selingue E, Geffroy F, Marques F, Cerqueira J, Sousa JC, Boumezbeur F, Bottlaender M, Jay TM, Cachia A, Sousa, Mériaux S, 2019. The SIGMA rat brain templates and atlases for multimodal MRI data analysis and visualization. Nat. Commun 10, 5699. [PubMed: 31836716]
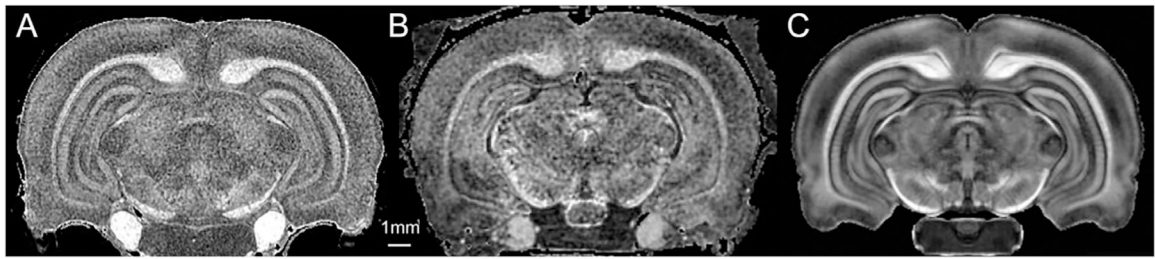
Fig. 1.
FA images demonstrating improvement in contrast to noise A) 50 um spatial resolution from Johnson et al 2012 (Johnson et al., 2012); B) 78 um spatial resolution from Papp et al (2014) (Papp et al., 2014); C) 50 um spatial resolution from the new template in this work.
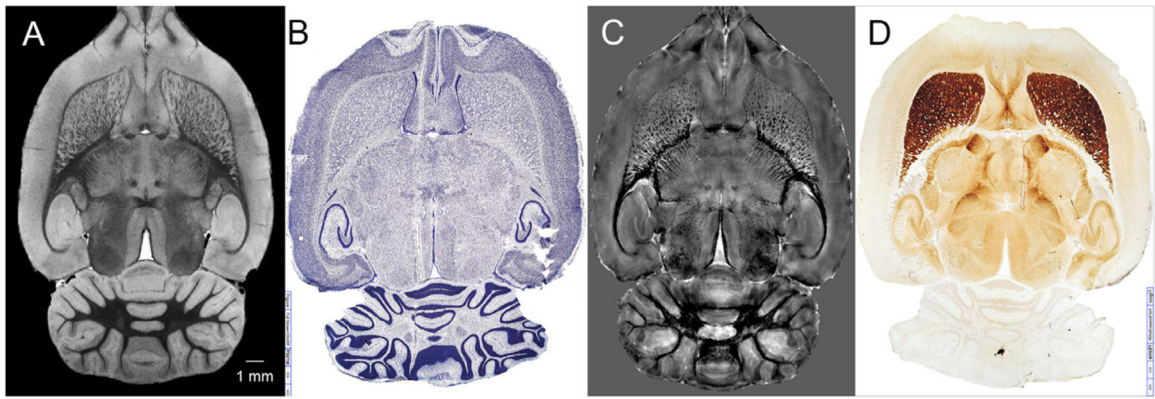
Fig. 2.
Comparison of (A) MGRE; (B) Nissl Plate 198 from Paxinos and Watson [1.] (used with permission); (C) Quantitative susceptibility map; (D) Acetylcholinesterase Plate 199 from Paxinos and Watson (used with permission). A, B, and C are at the same level. D is at an adjacent level in the histological series used to generate the Paxinos and Watson atlas.
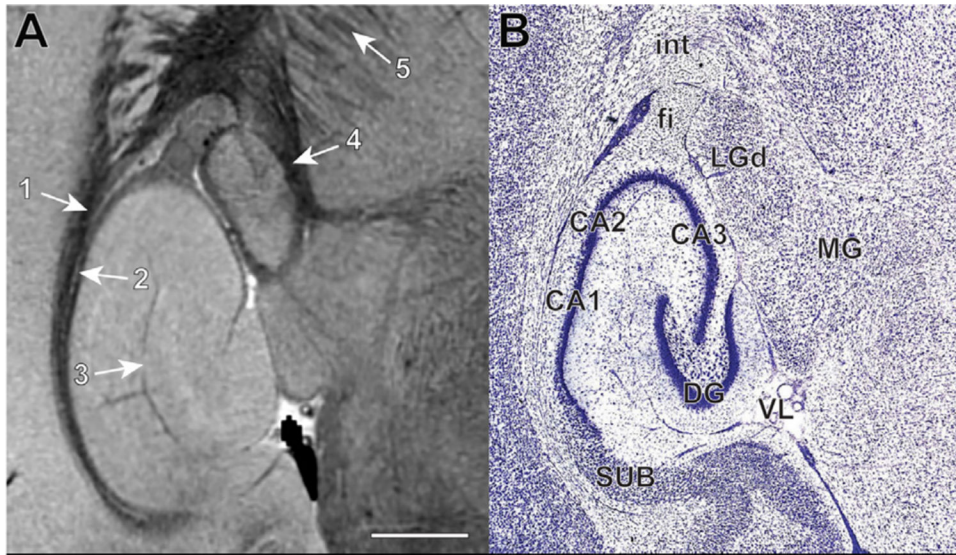
Fig. 3.
A magnified comparison of sections from Figure 1A and B through the hippocampus. (A)
MGRE image; 1) external capsule; 2) alveus; 3) hippocampal fissure; 4) optic radiation;
5) axon fascicles in the ventral-posterior thalamus; scale bar = 1 mm. (B) Nissl section;
CA1-CA3, subdivisions of the hippocampus (Ammon's horn fields, 1–3); DG, dentate
gyrus; fi, fimbria; int; internal capsule; LGd, dorsal part of the lateral geniculate complex of
the thalamus; MG, medial geniculate complex of the thalamus; SUB, subiculum; VL, lateral
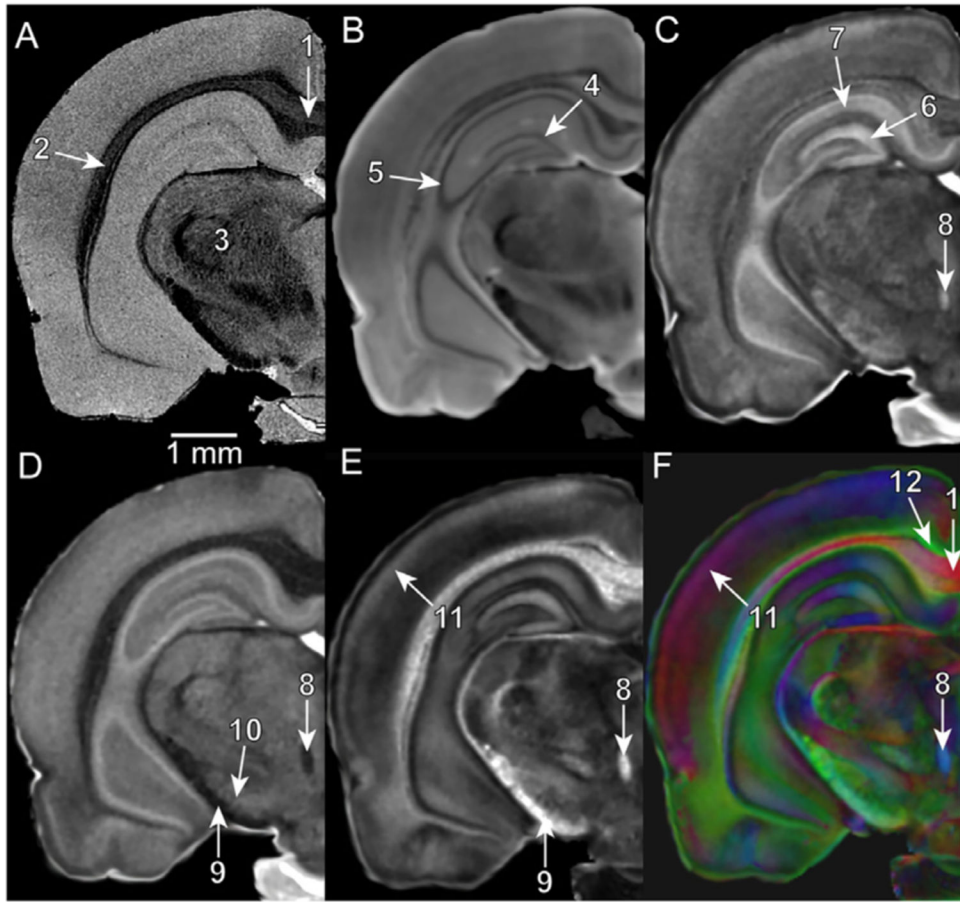ventricle.

Fig. 4.
Multi contrast images showing a coronal section through the hippocampus at bregma −4.68 mm. (A) MGRE; (B) DWI; (C) AD; (D) RD; (E) QA; (F) clrQA. 1) corpus callosum; 2) external capsule; 3) bundles of axon fascicles penetrating diencephalic (thalamic) gray matter; 4) granule cell layer of the dentate gyrus; 5) pyramidal cell layer of hippocampal field CA3; 6) molecular layer of the dentate gyrus; 7) stratum radiatum of hippocampal field CA1; 8) fasciculus retroflexus; 9) cerebral peduncle; 10) substantia nigra, reticular part; 11) neocortex, layer 2/3; 12) cingulum bundle.
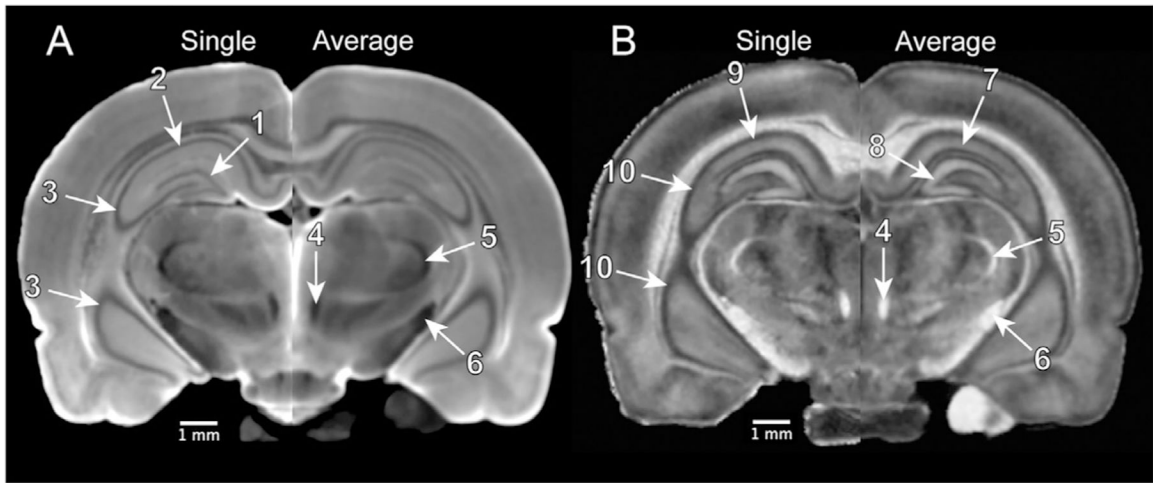
Fig. 5.

Comparison of coronal sections from (A) DWI and (B) QA for the single specimen (left side of section) and the average (n=6) (right side of section). The average images show some blurring in anatomical boundaries but improved signal-to-noise, in comparison to the single specimen. 1) granule cell layer of the dentate gyrus; 2) pyramidal cell layer of hippocampal field CA1; 3) pyramidal cell layer of hippocampal field CA3; 4) fasciculus retroflexus; 5) external medullary lamina of the thalamus; 6) cerebral peduncle; 7) stratum radiatum of hippocampal field CA1; 8) molecular layer of the dentate gyrus; 9) stratum oriens of hippocampal field CA1; 10) stratum oriens of hippocampal field CA3.
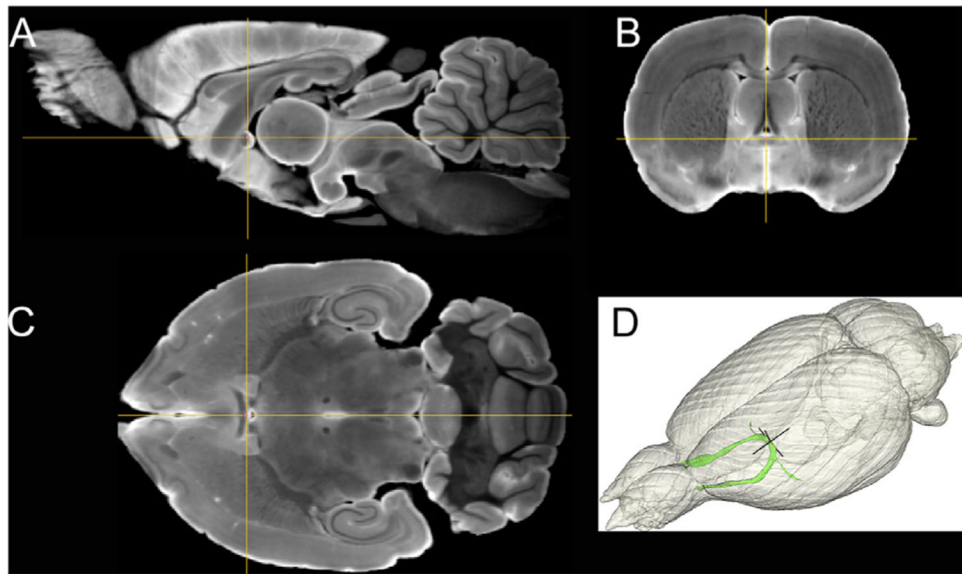
Fig. 6.
Origin for the atlas at the midline and juncture between anterior and posterior segments of the anterior commissure which is seen most easily in (A) the sagittal section of the DWI volume; (B) the coronal section; and (C) The axial section. (D) Volume rendered imaging showing origin at the anterior commissure.
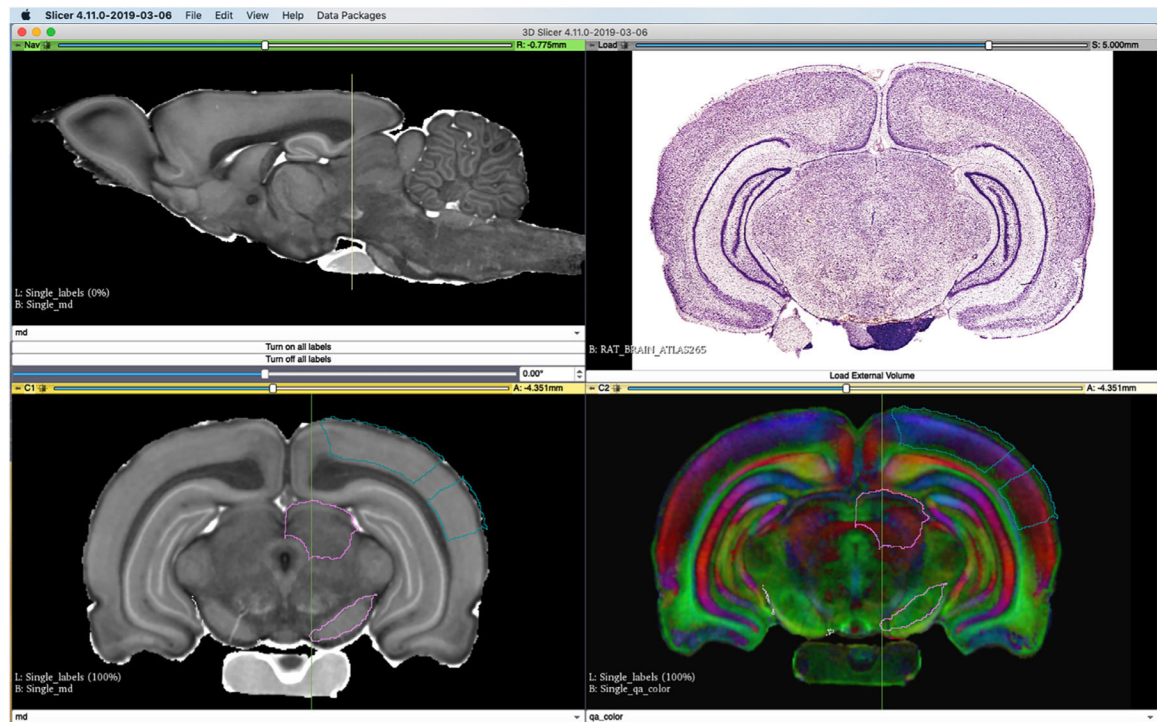
Fig. 7.
Screen capture of the 3D Slicer atlas application that supports interactive exploration of the multimodal data set. The average rat brain template is displayed. The sagittal MD (upper left) provides anatomic context for definition of slice location and angle of the coronal slices displayed in lower panes, both of which may be adjusted interactively by repositioning the sliders under the image. Two different contrasts (MD and clrQA) from a selection of available contrasts (AD, ADC, b0, clrQA, clrTDI, DWI, FA, GRE, grayTDI, MD, QA, QSM, RD) are shown in lower left and lower right, respectively. The application allows the user to upload images for comparison in the upper right pane. In this case, a representative Nissl section from Paxinos and Watson (Paxinos and Watson, 2013) (used with permission) has been loaded to demonstrate how one can interactively positional the atlas planes to match the section of interest. Selecting a region with the mouse, highlights the boundary of the neuroanatomical region (delineation) and provides the name in the 3D Slicer annotation pane (not shown).
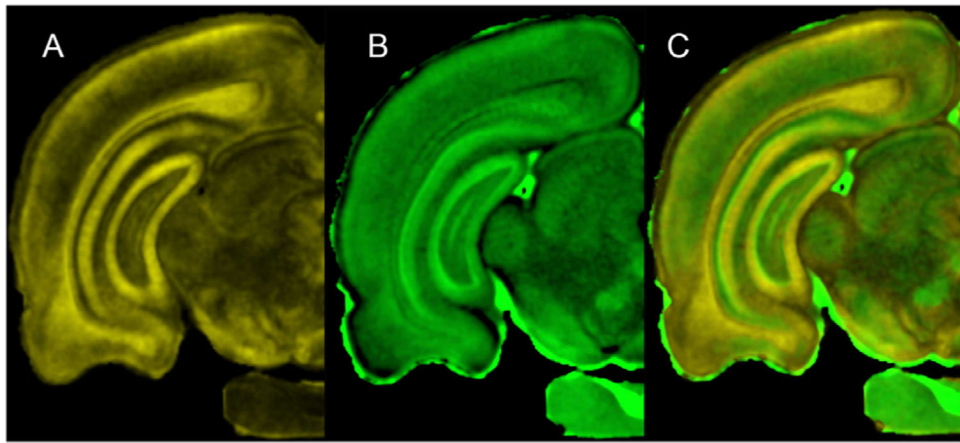
Fig. 8.
Different MR contrasts of the same (coronal) brain slice (corresponding to bregma −6.12 mm) are combined to generate unique views of neuroanatomical structure. (A) QA image. (B) AD image. (C) Combined view of QA and AD images. 1) external capsule (high QA signal); 2) region of the alveus/stratum oriens of hippocampal field CA1 (low QA signal); 3) stratum radiatum of hippocampal field CA1 (high QA signal); 4) molecular layer of the dentate gyrus (high QA signal); 5) stratum lacunosum-moleculare of hippocampal field CA1 (low QA signal); 6) granule cell layer of the dentate gyrus (high AD signal).
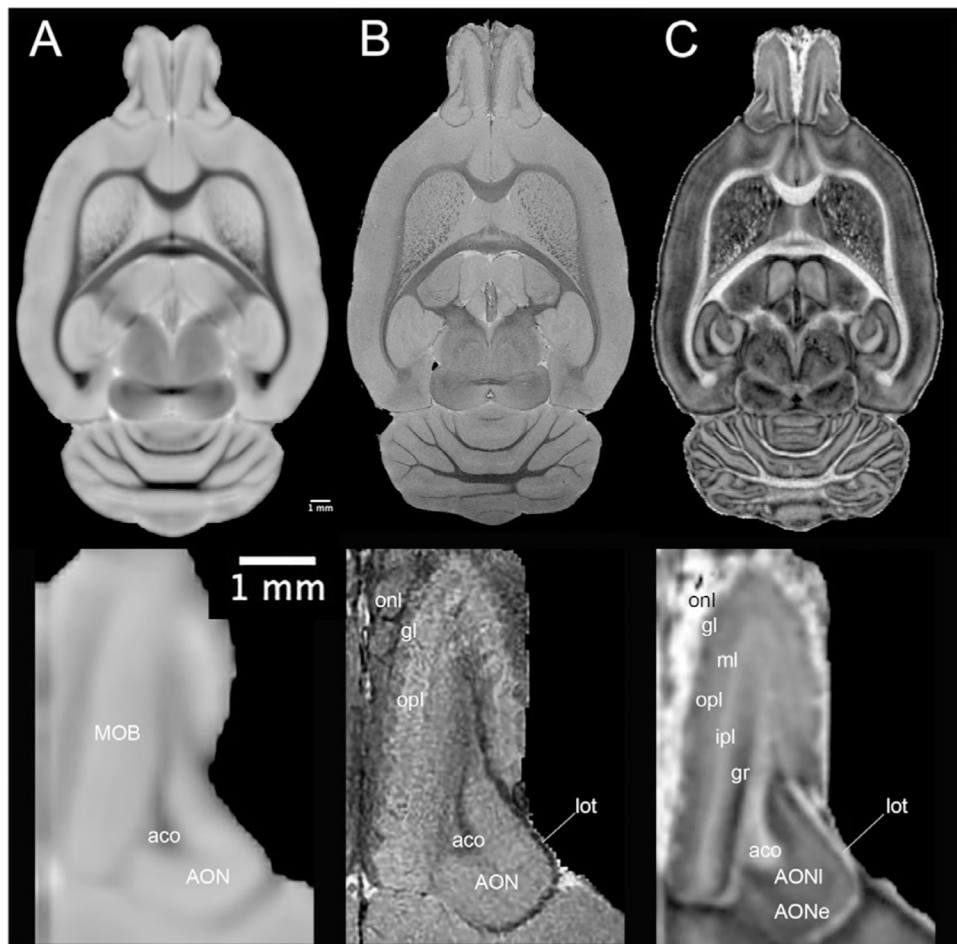
Fig. 9.
Comparison of the same axial plane from the SIGMA atlas (Barrière et al., 2019) and the present work. (A) The average MGRE data from the SIGMA atlas with voxel resolution @ $90 \times 90 \times 180$ um^3 and voxel volume of 1.5×10^{-3} mm^3. (B) The first echo from the MGRE image in our new template with voxel resolution @ $25 \times 25 \times 25$ um^3 and voxel volume of 1.5×10^{-5} mm^3. (C) The QA image in this new template with voxel resolution @ $50 \times 50 \times 50$ um and voxel volume of 1.25×10^{-4}. Lower row of panels provides higher magnification view of the rostral telencephalon highlighting the main olfactory bulb and the anterior olfactory nucleus. The MGRE image (B) shows more laminar structure in the main olfactory bulb and greater definition of the lateral olfactory tract than what is visible in the SIGMA atlas. Additional laminar features of the main olfactory bulb are evident in the QA image. Abbreviations: aco, anterior commissure, olfactory limb; AON, anterior olfactory nucleus; AONe, anterior olfactory nucleus, external part; AONl, anterior olfactory nucleus, lateral part; lot, lateral olfactory tract; gl, main olfactory bulb – glomerular layer; gr, main olfactory bulb – granule layer; ipl, main olfactory bulb – inner plexiform layer; ml, main olfactory bulb – mitral layer; onl, olfactory nerve layer of main olfactory bulb; opl, main olfactory bulb – outer plexiform layer.

Table 1

Previous atlases of the rat brain. Abbreviations used in the table: T1-spin lattice relaxation time; T2-spin spin relaxation time-decay in a spin echo sequence; T2*-decay in a gradient echo sequence; QSM-quantitative susceptibility map (Argyridis et al., 2013); DWI-diffusion weighted image; AD-axial diffusivity; RD-radial diffusivity; MD-mean diffusivity; FA-fractional anisotropy (Basser and Pierpaoli, 1996); ClrFA-color encoded fractional anisotropy (Mori and Zhang, 2006);QA-quantitative anisotropy (Yeh et al., 2010); ClrQA-color encoded quantitative anisotropy.

Reference	In Vivo/Ex Vivo	Spatial Resolution (um)	Voxel (mm³)	Contrasts	Labels
Paxinos and Watson 2013 (Paxinos and Watson, 2013)	Ex Vivo N=1	$1 \times 1 \times 40 \times 160$ $1 \times 1 \times 40 \times 220$	4×10^{-8}	Cressyl Violet Ache	>800
Johnson et al. 1987 (Johnson et al., 1987)	Ex Vivo N=1	$115 \times 115 \times 1200$	0.016	T1	<20
Schweinhardt P 2003 (Schweinhardt et al., 2003)	In Vivo N=5	$117 \times 117 \times 500$	.007	T2	28
Schwarz et al. 2006 (Schwarz et al., 2006)	In Vivo N=97	$156 \times 156 \times 1000$	.02	T2	39
Nie et al. 2013 (Nie et al., 2013)	In Vivo N=21	$140 \times 140 \times 300$	.006	T2	PW
Lancelot et al. 2014 (Lancelot et al., 2014)	In Vivo N=12	$100 \times 100 \times 400$	.004	T2	27
Wisner et al. 2016 (Wisner et al., 2016)	Ex Vivo N=2	$50 \times 50 \times 200$	.0005	Spin Density	PW
Barriere et al. 2019 (Barriere et al., 2019)	In Vivo Ex Vivo	$150 \times 150 \times 300$ $90 \times 90 \times 180$	.006 .001	T2 T2*	61
Goerzen et al. 2019 (Goerzen et al., 2019)	In Vivo N=41	$114 \times 114 \times 114$	.001	T2	71
Figini et al. 2015 (Figini et al., 2015)	In Vivo N=10	T2: $133 \times 133 \times 580$ DTI: $176 \times 176 \times 580$	.01 .02	T2	28
Veraart et al. 2011 (Veraart et al., 2011)	Ex Vivo	$88 \times 88 \times 88$	.0007	DWI,ClrFA, FA, T2*	14
Papp et al. 2014 (Papp et al., 2014)	Ex Vivo N=1	T2*:$39 \times 39 \times 39$ DTI:$78 \times 78 \times 78$	.00006 .0005	ADC, b0, ClrFA, DWI, FA, T2*	76
Kjonigsen et al. 2015 (Kjonigsen et al., 2015)	Ex Vivo N=1	T2*:$39 \times 39 \times 39$ DTI:$78 \times 78 \times 78$	.00006 .0005	ADC, b0, ClrFA, DWI,FA, T2*,	79
Osen et al. 2019 (Osen et al., 2019)	Ex Vivo N=1	T2*:$39 \times 39 \times 39$ DTI:$78 \times 78 \times 78$	.00006 .0005	ADC, b0, ClrFA, DWI, FA, T2*,	118
Johnson et al. 2012 (Johnson et al., 2012)	Ex Vivo N=5	T2*:$25 \times 25 \times 25$ DTI: $50 \times 50 \times 50$	1.6×10^{-5} 1.25×10^{-4}	ADC, ClrFA, DWI, FA, RD, T2*,	21
Calabrese et al. 2013[4]	Ex Vivo N=45	T2*:$25 \times 25 \times 25$ DTI: $50 \times 50 \times 50$	1.6×10^{-5} 1.25×10^{-4}	ADC, ClrFA, DWI, FA, RD, T2*,	26

Reference	In Vivo/Ex Vivo	Spatial Resolution (um)	Voxel (mm³)	Contrasts	Labels
Paxinos et al. 2015 (Paxinos et al., 2015)	Ex Vivo N=5	T2*:25 × 25 × 250 DTI: 50 × 50 × 250	1.6×10^{-5} 1.25×10^{-4}	ClrFA, DWI, T2*,	~700
This work	Ex Vivo N=6	T2*: 25 × 25 × 25 DTI: 50 × 50 × 50	1.6×10^{-5} 1.25×10^{-4}	AD, b0, ClrQA, ClrTDI, DWI, FA, MD, QA, QSM, RD, T2*, TDI	360